Reports

Sea-Level Solar Radiation in the Biologically Active Spectrum

Abstract. *Calculations show a significant depletion of ultraviolet and visible radiation due to absorption and scattering by particulates and cloud drops for a fixed amount of ozone.*

It is possible that the presence of a fleet of supersonic transport planes in the stratosphere can lead to a significant decrease in the ozone content of the terrestrial atmosphere (*1*). Consequently, considerable attention has been given in recent years to the biospheric effects of an increase in the ground-level ultraviolet flux due to a hypothetical decrease in the atmospheric ozone content. Because of the difficulty of carrying out controlled experiments in the atmosphere, it is customary to evaluate a change in the ground-level ultraviolet flux due to a change in the ozone content by computer modeling. Cutchis (*2*) has reported the results of his numerical simulations to demonstrate the effect of a stratospheric ozone depletion on the ultraviolet solar flux received at the ground. His atmospheric model contains a vertical distribution of ozone as observed under average mid-latitude summer conditions but is otherwise free of dust (aerosol) and clouds (water drops).

The actual dose of ultraviolet radiation which is received at the surface under present mid-latitude summer conditions is smaller than that computed by Cutchis (*2*), who used tables of Dave and Furukawa (*3*) for the unperturbed stratospheric conditions. This is so because there is an additional depletion of radiation due to the scattering and absorption by aerosol and water drops.

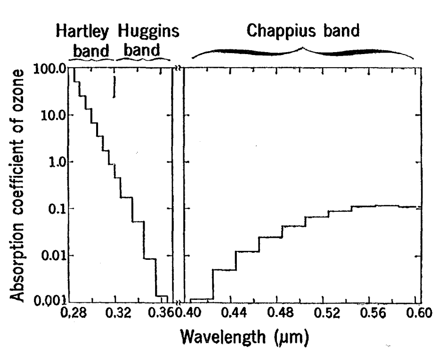

Fig. 1. Variation of the absorption coefficient of ozone as a function of wavelength as used in these computations.

In this report we describe some results of extensive numerical simulations showing the effect of changes in aerosol characteristics on the total (direct solar radiation plus diffuse sky radiation) flux in the spectral region from 0.29 to 0.06 μm received at sea level when the ozone content of the atmosphere remains unchanged. We obtained these results by taking into account all orders of scattering in one-dimensional, nonhomogeneous atmospheric models with realistic height distributions of ozone, aerosol, and water drops. Models used in this investigation vary from a model with ozone but no dust or clouds at one extreme to several models with climatic cloud cover (defined below) and high concentrations of aerosol at the other.

Although the action spectrum of biological effects such as erythema falls in the spectral region from 0.29 to 0.34 μm, the extension of the spectral limit through the visible to 0.6 μm is justified on several counts. Human skin shows some significant absorption for radiation with wavelengths as large as 0.6 μm (*4*). Since the effects in the visible region are easily observable, one can assess the relative effect of dust in the ultraviolet with respect to the visible. Finally, the long-wavelength limit of the solar spectrum for various other biological effects (for example, photosynthesis) extends far into the visible.

The solar spectrum of interest was divided into 23 unequal spectral intervals as follows: 0.290 to 0.325 μm (for a 0.005-μm interval), 0.325 to 0.365 μm (for a 0.01-μm interval), and 0.365 to 0.605 μm (for a 0.02-μm interval). We determined the boundaries of these spectral intervals, as well as the mean values of the absorption coefficient (see Fig. 1) of 1 cm of ozone at normal temperature and pressure required as input in our computations somewhat subjectively, after plotting high-resolution data as a function of wavelength λ (*5*). Values of the normal optical thickness due to Rayleigh scattering by air molecules as used in our radiation transfer calculations for the spectral intervals listed above can be found elsewhere (*6*). This optical thickness, which varies as λ^{-4}, has a value of 1.36 at 0.29 μm and a value of 0.07 at 0.60 μm. The typical aerosol optical thickness in this spectral region is 0.10 for average aerosol concentrations.

The variation of the ozone density as a function of the height used is shown in Fig. 2. This ozone distribution corresponds to average mid-latitude summer conditions (*7*) and contains 0.318 atm-cm of total ozone in a 1-cm^2 column of the atmosphere.

For our work, we have chosen the modified gamma functions "Haze L" and "Cloud C1" for representing the size distribution of aerosol particles and cloud water drops, respectively (*8*). The manner in which these distributions reflect realistic aerosol concentrations in the atmosphere is discussed in (*8*). The values of the lower and upper cutoffs for particle radius as used in our computations are 0.001

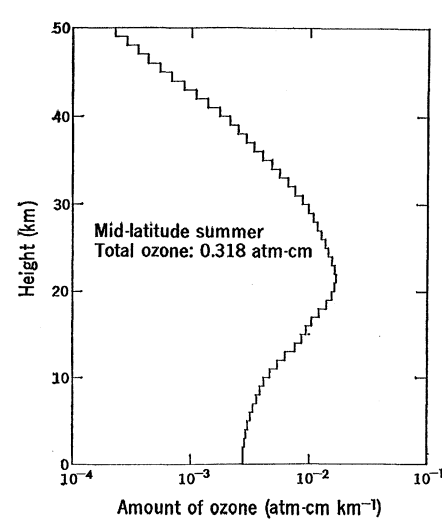

Fig. 2. Vertical distribution of the atmospheric ozone as used in these computations.

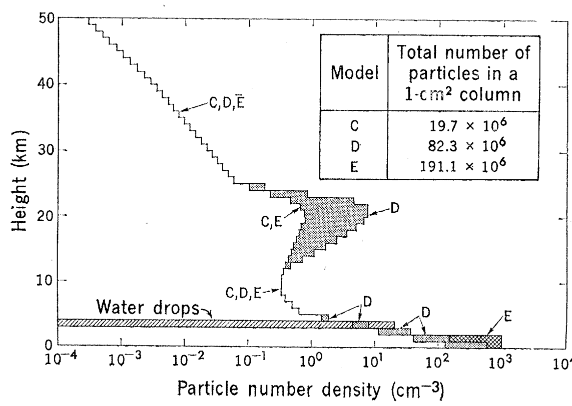

Fig. 3. Vertical distribution of the atmospheric aerosol particles and of the liquid water drops as used in these computations. The vertical distribution designated model C is given by the solid line closest to the ordinate. Model D is obtained after adding all the shaded areas to the model C curve, and model E is obtained after adding shaded and hatched areas between 0 and 2 km to the curve of model C.

and 7.0 μm, respectively, for the Haze L function and 2.0 and 11.0 μm, respectively, for the Cloud C1 function. The mode radii for these two distributions (at which the distribution has its maximum value) are 0.07 and 4.0 μm, respectively.

In order to simulate the effect of increasing aerosol due to a combination of man-made and natural (volcanic) sources, we have defined three aerosol height distributions in Fig. 3. The height distribution designated model C is given by the solid line closest to the ordinate. It represents typical, average atmospheric conditions, and has about 20×10^6 particles in a 1-cm^2 atmospheric column above the ground level. The second height distribution, designated model D, is obtained by increasing the aerosol content of the Junge layer (*9*) (12- to 22-km region) and of the lower troposphere (0- to 5-km region) as shown by the shaded areas in Fig. 3. Model D, representing high aerosol concentrations on a global scale, contains about 82×10^6 particles in a 1-cm^2 atmospheric column above the ground. The third height distribution (model E) is obtained after increasing the aerosol content of the 0- to 2-km region of model C by an order of magnitude (shaded area plus hatched area of Fig. 3). This very high concentration of aerosol (191×10^6 particles in a 1-cm^2 column of the atmosphere above the ground) is expected to represent a typical case of moderate urban pollution with average conditions aloft.

For simulating the effect of climatic cloud cover in this one-dimensional model, we have introduced a stratus cloud layer between 3 and 4 km (Fig. 3). This model cloud, containing 2.05×10^6 drops in a 1-cm^2 column and a liquid water content of 0.013 g m^{-3}, has a value of 33.2 percent for its spectrally integrated spherical albedo (the reflectivity of the planet's disk) when a value of $1.34 - 0.00i$ is assumed for the wavelength-independent refractive index of water (*10*). This albedo is close to that observed by satellite for the earth with average cloud cover (*11*).

The scattering and absorption cross sections of a unit volume of aerosol or water drops, and the normalized Legendre coefficients needed for representing the scattering phase function of the volume, were computed for each of the 23 wavelengths listed above, and for five different values of refractive indices used in our investigations, from corresponding values of the quantities for spherical particles with the following discrete values of the size parameter x: 0.02 to 10.00 (for a 0.02 interval in x), and 10.0 to 250.0 (for a 0.1 interval in x), where $x = 2\pi r \lambda^{-1}$ (r is the particle radius).

Information presented in the preceding paragraphs was used to develop ten different atmospheric models described in Table 1. A zero value for the imaginary part of the refractive index implies that the aerosol particles by themselves do not absorb any energy. A value of 0.01 for the imaginary part of the refractive index corresponds to the case of a weak absorption of energy by aerosol. A value of $1.66 - 0.25i$ for the refractive index (model E3) represents a strong absorption by carbon aerosol (*12*). For models E1, E2, and E3, the particles above 2 km are assumed to be made of a material with a refractive index of $1.50 - 0.00i$. Results presented in this report are for the cases in which all models listed in Table 1 "rest" on a ground which absorbs all the energy incident upon it. Real surfaces have a reflectivity r ranging from about 0.05 for oceans to between 0.5 and 0.6 for snowfields. A nonzero reflectivity will generally slightly increase the amount of diffuse sky radiation received at the ground as a result of backscattering of the reflected flux (*6, 10*).

For all models except E1, E2, and E3, the procedure used for obtaining a solution of the basic transfer equation for a nonhomogeneous atmospheric model is a direct numerical solution of the spherical harmonics approximation to the azimuth-independent component of the intensity in the equation of radiative transfer (*10, 13*).

For the E series models, the atmosphere was divided into two basic layers, namely, a 0- to 2-km region, the so-called boundary layer, and a 2- to 50-km region, the so-called free atmosphere (*14*). The direct and diffuse radiation incident on the top of the boundary layer for a given wavelength and position of the sun was obtained from the work of Braslau and Dave (*6*). We evaluated the transfer of this incident radiation through the bound-

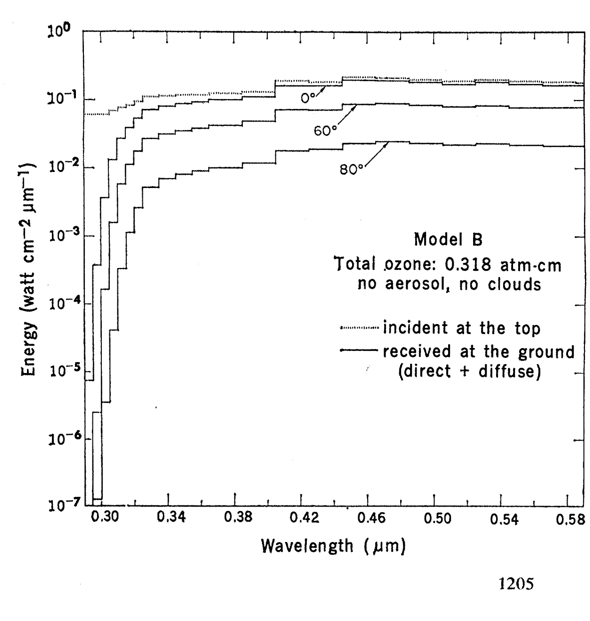

Fig. 4. Spectral distribution of the solar flux normally incident at the top of the atmosphere (dotted curve), and of the total (that is, direct solar radiation and diffuse sky radiation) flux received at the ground for three different zenith angles of the sun. Model B: midlatitude summer distribution of ozone described in Fig. 2; no aerosol or water drops; ground reflectivity $R = 0$.

ary layer by using an iterative technique (*6*, *10*).

Both computational procedures provide values of the rate of flow of energy or flux (in watts per square centimeter per micrometer) passing normally through a unit horizontal surface at kilometer intervals along the vertical. These values are obtained for various models as a function of wavelength, and for several values of θ_0, the zenith angle of the sun.

In Fig. 4 we present spectral distributions of the solar flux incident at the top of the atmosphere (*5*) (dotted curve) and of the rate of energy flow (flux) through a unit horizontal surface at the ground for $\theta_0 = 0°$, 60°, and 80°. The ground-level fluxes are for model B (see Table 1). The energy received at the ground decreases with the increase in the zenith angle of the sun, and also with the decrease in the wavelength of the radiation under investigation. The strong absorption in the Hartley-Huggins band of ozone (Fig. 1) is the cause of the loss of ground-level flux in the short-wavelength part of the spectral region from 0.29 to 0.34 μm.

The results shown in Fig. 4 give the energy flow due to the direct solar radiation as well as the diffuse sky radiation. For the sun at local zenith ($\theta_0 = 0°$), the direct component is greater than the diffuse component for all wavelengths. However, they differ by about an order of magnitude in the visible but are practically the same in the ultraviolet region. For $\theta_0 = 60°$ and 80°, the direct component is greater than the corresponding diffuse component only if the wavelengths are greater than 0.35 and 0.47 μm, respectively.

In the preceding paragraphs, we found that the spectral and diurnal variations of the rate of flow of energy through a unit horizontal area at the

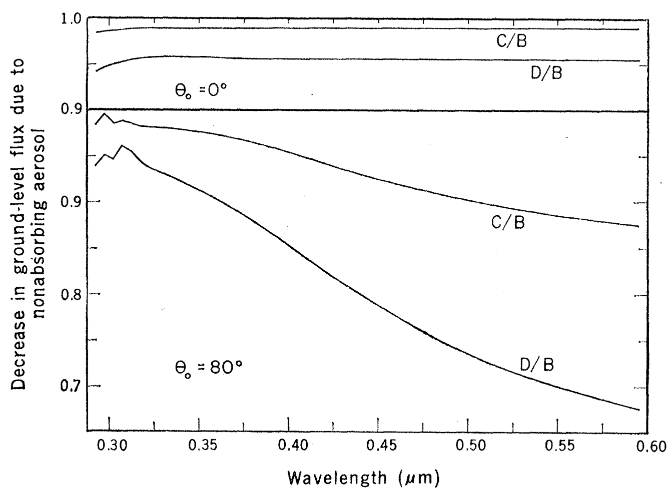

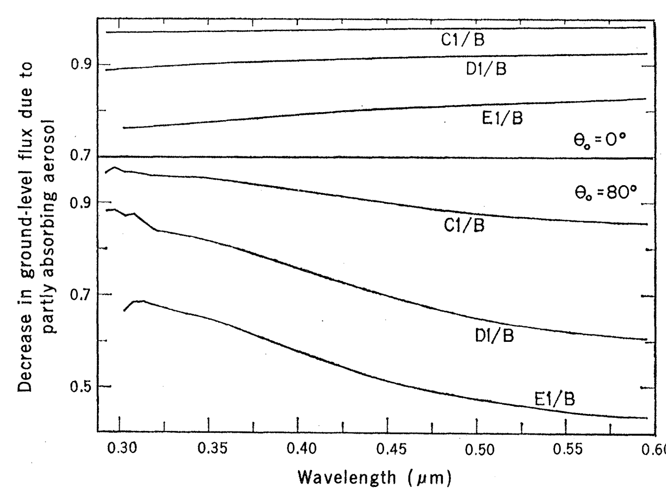

Fig. 5 (left). Spectral variations of the decrease in ground-level flux (direct plus diffuse) due to the presence of nonabsorbing aerosol. Model B: ozone only; model C: ozone and average aerosol concentrations; model D: ozone and high aerosol concentrations. Fig. 6 (right). Spectral variations of the decrease in ground-level flux (direct plus diffuse) due to the presence of partly absorbing aerosol. Model B: ozone only; model C1: ozone and average aerosol concentrations; model D1: ozone and high aerosol concentrations; model E1: ozone and very high aerosol concentrations. The refractive index of the partly absorbing aerosol material $m = 1.50 - 0.01i$.

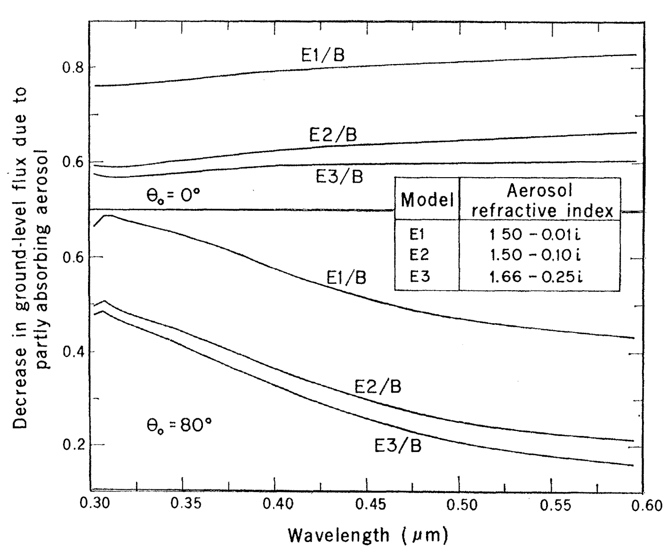

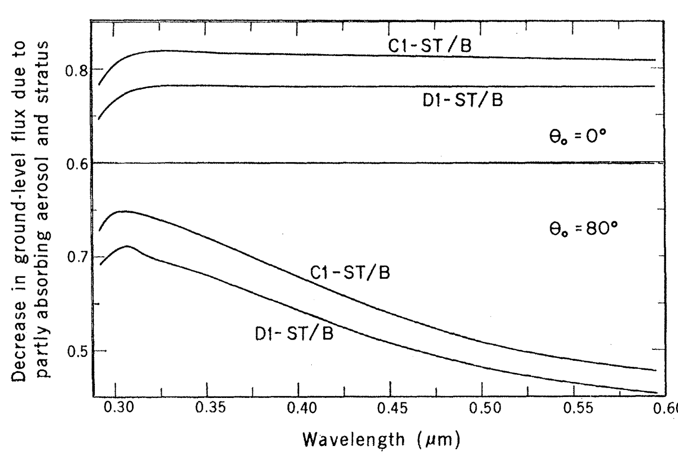

Fig. 7 (left). Spectral variations of the decrease in ground-level flux (direct plus diffuse) due to the presence of partly absorbing aerosol. Model B: ozone only; models E1, E2, and E3: ozone and very high aerosol concentrations. Fig. 8 (right). Spectral variations of the decrease in ground-level flux (direct plus diffuse) due to the presence of partly absorbing aerosol and a stratus cloud layer between 3 and 4 km. Model B: ozone only; model C1-ST: ozone, stratus layer, and average aerosol concentration; model D1-ST: ozone, stratus layer, and high aerosol concentration. The refractive index of the partly absorbing aerosol material $m = 1.50 - 0.01i$.

bottom of the atmosphere extend over six orders of magnitude. On the other hand, we found that the changes in these quantities due to the presence of aerosol or cloud layers of the types used in our investigations, or both, are no more than an order of magnitude at the most. Hence, for the sake of clarity and simplicity of presentation, we have considered it appropriate to discuss the variations of the ratio $[\rho(\lambda,\theta_0)]$ of the rate of flow of energy through a unit horizontal area at the bottom of model X to that for model B, as a function of λ and θ_0. In other words, the ratio $\rho(\lambda,\theta_0)$ for the X/B case represents a decrease in the ground-level flux due to impurities added in model B to arrive at model X.

Table 1. Atmospheric models.

Model	Ozone absorption	Aerosol concentration	Aerosol refractive index	Stratus clouds
B	Yes	None		No
C	Yes	Average	$1.50 - 0.00i$	No
D	Yes	High	$1.50 - 0.00i$	No
C1	Yes	Average	$1.50 - 0.01i$	No
D1	Yes	High	$1.50 - 0.01i$	No
E1	Yes	Very high	$1.50 - 0.01i$	No
E2	Yes	Very high	$1.50 - 0.10i$	No
E3	Yes	Very high	$1.66 - 0.25i$	No
C1-ST	Yes	Average	$1.50 - 0.01i$	Yes
D1-ST	Yes	High	$1.50 - 0.01i$	Yes

Figure 5 shows the effect of adding average (model C) and high (model D) concentrations of nonabsorbing aerosol on the spectral distribution of the total (direct plus diffuse) flux emerging at the bottom of the atmosphere. For $\theta_0 = 0°$ (upper section of Fig. 5), the ratio $\rho(\lambda,0°)$ increases from 0.986 to 0.990 with increasing wavelength for the C/B case, and from 0.943 to 0.957 for the D/B case with most of the increase confined around the 0.30-μm region. On the other hand, the presence of nonabsorbing aerosol affects the visible radiation more compared to the ultraviolet when the sun is very near the horizon. The ratio $\rho(\lambda,80°)$ (lower section of Fig. 5) for the C/B case decreases rapidly from 0.99 to 0.88 as λ increases from 0.3 to 0.6 μm. The introduction of large amounts of aerosol into model B results in about a 5 percent decrease in the green-red part of the spectrum. This spectrally distinguishable effect of the nonabsorbing aerosol is due to a relative increase in the diffuse component of the energy received at the ground.

The variations of the ratio $\rho(\lambda,\theta_0)$ as a function of λ are presented in Fig. 6 for $\theta_0 = 0°$ (upper section) and for $\theta_0 = 80°$ (lower section) when average (model C1), high (model D1), and very high (model E1) concentrations of weakly absorbing aerosol are added to model B. For $\theta_0 = 0°$, this ratio now gradually increases with an increase of wavelength for all three cases. The presence of the average amount of dust decreases the ground-level ultraviolet flux by about 3 percent, but further fourfold (D1/B case) and tenfold (El/B case) increases in dust content reduce the ground-level ultraviolet flux by about 11 and 24 percent, respectively. For $\theta_0 = 80°$, the variations are still larger.

A comparison of the results presented in Fig. 6 for the partly absorbing aerosol with those presented in Fig. 5 for the nonabsorbing aerosol shows that even a weak absorption by aerosol material decreases the energy received at the ground by a very significant amount, especially if the atmospheric dust content is high and the sun is low.

The variations of the ratio $\rho(\lambda,\theta_0)$ as a function of λ are shown in Fig. 7 for the cases E1/B, E2/B, and E3/B. As mentioned earlier, all these three models contain very high concentrations of aerosol near the ground with absorption by aerosol material increasing from model E1 through model E3. An increase in the imaginary part of the refractive index of the aerosol material from 0.01 to 0.10 results in a very strong decrease (from about 20 to 30 percent to up to a factor of 2 or more in some cases) in the amount of energy received at the surface. A further increase in the value of the imaginary part from 0.10 to 0.25 results in only a small decrease in the values of the ground-level fluxes. An increase in the real part of the refractive index (from 1.50 for models E1 and E2 to 1.66 for model E3) cannot be expected to affect values of $\rho(\lambda,\theta_0)$ in any significant manner.

Variations of $\rho(\lambda,\theta_0)$ as a function of λ are shown in Fig. 8 for the cases C1-ST/B and D1-ST/B to display the combined effect of a climatic cloud cover and partly absorbing aerosol on the spectral distribution of energy received at the ground. The results presented in this diagram should be studied in conjunction with those presented in Fig. 6. It suffices to say that the presence of even a moderately thin cloud layer results in a significant decrease in the ground-level flux; for example, the ratio $\rho(0.2925\ \mu\text{m}, 0°)$ has a value of 0.972 for the C1/B case but a value of 0.769 for the C1-ST/B case.

The results presented here show a strong and variable effect of the atmospheric aerosol and clouds on the spectral distribution of the solar energy received at the ground. The primary factors determining the magnitude of these effects are the wavelength of the radiation under investigation, the position of the sun, the atmospheric aerosol content, the absorbing characteristics of the aerosol substance, and the presence as well as the nature of the cloud layer. It has been shown that, even when the atmospheric ozone content is held constant, life in the biosphere and especially that in and around urban areas is being subjected to significantly smaller doses of ultraviolet and visible radiations than those computed from atmospheric models with Rayleigh scattering only (*2*). Since a large fraction of the ultraviolet radiation received at the ground is in the form of diffuse skylight, the relationship between the amount of stratospheric ozone and the solar energy received at the surface can be a complicated one, depending upon several of the parameters listed above and on additional ones such as the height and size distributions of aerosol and water drop clouds. Thus, in order to evaluate the biospheric effects of a supersonic fleet, one must carry out a comprehensive radiation transfer study with the expected compositions of the stratosphere in addition to the possible conditions that are likely to be encountered in the troposphere at that time.

PAUL HALPERN
J. V. DAVE
IBM Scientific Center, 2670 Hanover Street, Palo Alto, California 94304
NORMAN BRASLAU
IBM T. J. Watson Research Center, Yorktown Heights, New York 10598

References

1. A. J. Broderick, in *Proceedings of the Second Conference on the Climatic Impact Assessment Program, November 14–17, 1972* (Publication DOT-TSC-OST-73-4, National Technical Information Service, Springfield, Va., 1973).
2. P. Cutchis, *Science* **184**, 13 (1974).
3. J. V. Dave and P. M. Furukawa, *Meteorol. Monogr.* **7** (No. 29), 1 (1966).
4. B. E. Johnson, F. Daniels, Jr., I. A. Magnus, in *Photophysiology, Current Topics*, A. C. Giese, Ed. (Academic Press, New York, 1968), vol. 4, p. 139.
5. J. N. Howard, J. I. F. King, P. R. Gast, in *Handbook of Geophysics* (Macmillan, New York, 1961), chap. 16.
6. N. Braslau and J. V. Dave, *Reports RC 4114, 4152, 4308* (IBM T. J. Watson Research Center, Yorktown Heights, N.Y., 1972–1973). See also N. Braslau and J. V. Dave, *J. Appl. Meteorol.* **12**, 601 (1973); *ibid.*, p. 616.
7. R. A. McClatchey, R. W. Fenn, J. E. A. Selby, J. S. Garing, F. E. Volz, *Rep. No. AFCRL-70-0527* (Air Force Cambridge Research Laboratories, Bedford, Mass., 1970).
8. D. Deirmendjian, *Electromagnetic Scattering on Atmospheric Polydispersions* (Elsevier, New York, 1969).
9. C. E. Junge, *Air Chemistry and Radioactivity* (Academic Press, New York, 1963).
10. J. V. Dave and N. Braslau, in preparation.
11. E. Raschke and W. R. Bandeen, *J. Appl. Meteorol.* **9**, 215 (1970).
12. J. T. Twitty and J. A. Weinman, *ibid.* **10**, 725 (1971).
13. J. V. Dave and J. Canosa, *J. Atmos. Sci.* **31**, 1089 (1974); J. V. Dave, *Rep. No. UCRL-51581* (Lawrence Livermore Laboratory, University of California, Livermore, 1974).
14. P. Halpern, thesis, University of California, Davis, in preparation.

23 August 1974

Skylab Radar Altimeter: Short-Wavelength Perturbations Detected in Ocean Surface Profiles

Abstract. *Short-wavelength anomalies in sea surface topography, caused by the gravitational effects of major ocean bottom topographic features, have been detected by the radar altimeter aboard Skylab. Some features, such as deep ocean trenches, seamounts, and escarpments, displace the ocean surface by as much as 15 meters over 100-kilometer wavelengths. This experiment demonstrates the potential of satellite altimetry for determining the ocean geoid and for mapping major features of the ocean bottom.*

We report here preliminary results from the Skylab radar altimeter which was part of the Earth Resources Experimental Package (EREP) aboard Skylab. This was the first in a series of altimeters planned to be placed in Earth orbit to determine both geodetic and oceanographic characteristics of the ocean surface. The primary purposes of the radar altimeter experiment were to determine the feasibility of using satellite altimetry to investigate geophysical phenomena and to obtain the necessary engineering data for the design of future satellite altimeter systems.

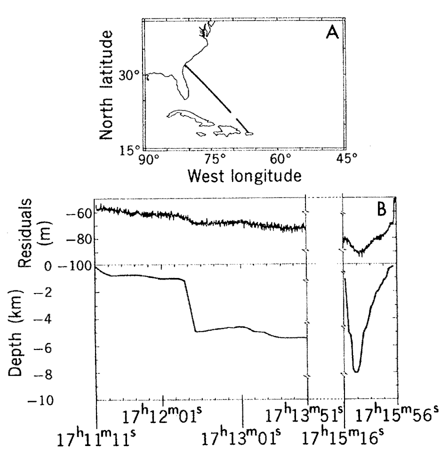

Fig. 1. (A) Subsatellite trace for EREP pass 4, SL-2, 4 June 1973. (B) Sea surface topography determined by altimeter, and the bottom topography beneath the subsatellite trace, showing the Blake Escarpment and the Puerto Rico Trench.

Skylab was placed into Earth orbit on 14 May 1973 at a mean altitude of 440 km and an inclination of 50 deg. More than 150 altitude data sets have been acquired during the three manned Skylab missions (SL-2, SL-3, and SL-4), and data gathered from SL-2 and SL-3 provide the data base for this investigation.

The radar altimeter was built by the General Electric Company, Ithaca, New York. It operates at a 13.9-Ghz frequency, transmits one of three selectable pulsewidths (20, 100, or 10 nsec) at a pulse repetition rate of 250 pulses per second, and has five different operating modes, three of which provide altitude measurements. The altitude data are recorded at a rate of eight samples per 1.04 seconds. Other characteristics of the altimeter are described in McGoogan (*1*) and McGoogan *et al.* (*2*).

The basic concept of altimetry is the utilization of a highly stable, moving reference system from which vertical measurements to the ocean surface are made. The orbiting Skylab, positioned by ground-tracking instrumentation, provides the stable reference surface, and the radar altimeter measures the distance from the reference orbit to the sea surface. The altimeter is basically a conventional tracking radar which tracks in range only. A narrow pulse is transmitted from the altimeter to the sea surface. The time interval from the transmit time to the half-power point of the leading edge of the return pulse is proportional to the altitude. These transmit times are measured with a closed-loop tracking system with bandwidths of a few hertz to follow the dynamics of the ocean surface. If the pulsewidth represents a time spread on the ocean surface that is less than the beamwidth, then either pulsewidth, sea state, or both will determine the footprint size. This footprint acts as a spatial filter that must be considered in analyzing surface features.

Factors considered in the calibration of the altitude measurements include the pointing of the antenna, pulsewidth or bandwidth changes (or both), in-flight calibration data, and atmospheric retardation. Prior to in-depth analysis, antenna pointing is assured to be within 0.5 deg of the nadir, since pointing errors produce bias errors in the altitude measurement. Altitude biases up to 15 m due to the switching of transmitted pulsewidths or receiver bandwidths, or both, are corrected for in the processing. The alti-

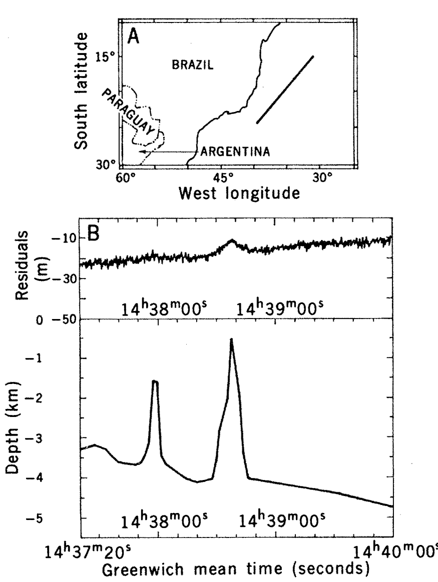

Fig. 2. (A) Subsatellite trace for EREP pass 11, SL-3, 2 September 1973. (B) Sea surface topography determined by altimeter, and the bottom topography beneath the subsatellite trace, showing seamounts off the east coast of Brazil.